IEEE Open Journal of the
Industrial Electronics Society

Received 21 July 2022; revised 1 September 2022; accepted 15 September 2022. Date of publication 21 September 2022; date of current version 17 October 2022. The review of this paper was arranged by Associate Editor X. Zhao.

Digital Object Identifier 10.1109/OJIES.2022.3208329

Nonlinear Current Control of Reluctance Synchronous Machines With Analytical Flux Linkage Prototype Functions

SHIH-WEI SU [1], HANNES BÖRNGEN [1] (Student Member, IEEE), CHRISTOPH M. HACKL [2] (Senior Member, IEEE), AND RALPH KENNEL [1] (Senior Member, IEEE)

[1]Chair of High-Power Converter Systems, Technical University of Munich, 80333 Munich, Germany
[2]Department of Electrical Engineering and Information Technology, Munich University of Applied Sciences, 80335 Munich, Germany

CORRESPONDING AUTHOR: CHRISTOPH M. HACKL (e-mail: christoph.hackl@hm.edu)

ABSTRACT The article proposes a nonlinear current control system of reluctance synchronous machines (RSMs) in combination with analytical flux linkage prototype functions. For highly nonlinear machines, such as RSMs, the magnetic characteristics change significantly throughout the whole operation range due to saturation and cross-coupling effects. Therefore, the current controller tuning must be adapted online to achieve a fast and accurate tracking performance. The proposed current controllers are derived based on the system theoretic concept of the exact input/output (I/O) linearization of the current dynamics. Thus, the nonlinear control system is simplified to an integrator which, in combination of proportional–integral controllers, can be tuned by means of pole placement similar to a phase-locked loop. For I/O linearization and control, the magnetic saturation and cross-coupling effects in the flux linkages and the differential inductances must be considered which is done by the utilization of analytical flux linkage prototype functions instead of lookup tables. The performance of the developed nonlinear current control system is validated by both, simulation and experimental results, for a highly nonlinear 1.5 kW RSM. The results underpin 1) the very high approximation accuracy and the continuity and differentiability of the flux linkage prototype functions over the whole operation range and 2) the very fast and accurate tracking performance of the nonlinear I/O control system.

INDEX TERMS Analytical flux linkage prototype functions, nonlinear current control, reluctance synchronous machine (RSM), saturation effects.

NOTATION

$\mathbb{N}, \mathbb{R}$: natural, real numbers. $\boldsymbol{x} := (x_1, \dots, x_n)^\top \in \mathbb{R}^n$: column vector, $n \in \mathbb{N}$ where "$^\top$" and ":=" denote "transposed" and "is defined as," respectively. $\boldsymbol{a}^\top \boldsymbol{b} := a_1 b_1 + \cdots + a_n b_n$: scalar product of vectors $\boldsymbol{a}$ and $\boldsymbol{b}$. $\|\boldsymbol{x}\| := \sqrt{\boldsymbol{x}^\top \boldsymbol{x}}$: Euclidean norm of $\boldsymbol{x}$. $\boldsymbol{X} \in \mathbb{R}^{n \times m}$: matrix with n rows and m columns. $\boldsymbol{I}_n := \mathrm{diag}(1, \dots, 1) \in \mathbb{R}^{n \times n}$: identity matrix. $f(t) \circ\!\!-\!\!\bullet\, f(s)$: Laplace transform $f(s)$ of a function $f(t)$. $\boldsymbol{T}_\mathrm{p}(\phi_\mathrm{p}) = \begin{bmatrix} \cos(\phi_\mathrm{p}) & -\sin(\phi_\mathrm{p}) \\ \sin(\phi_\mathrm{p}) & \cos(\phi_\mathrm{p}) \end{bmatrix}$: Park transformation matrix with angle $\phi_\mathrm{p} \in \mathbb{R}$ and $\boldsymbol{J} := \boldsymbol{T}_\mathrm{p}(\pi/2) = \begin{bmatrix} 0 & -1 \\ 1 & 0 \end{bmatrix}$: counterclockwise rotation matrix (by $\frac{\pi}{2}$).

I. INTRODUCTION

In recent years, reluctance synchronous machines (RSMs) have drawn attention from industry to their various applications due to their compact design, high efficiency, and reliability [1], [2], [3]. As both the efficiency requirements and the price of rare earth materials are increasingly rising, RSMs are considered as a viable alternative to induction machines (IMs) and permanent magnet synchronous machines (PMSMs). Moreover, without the need for windings and/or permanent magnets in the rotor, the simple and rigid rotor structure allows the operation under harsh environmental conditions.

However, RSMs possess extremely nonlinear magnetic characteristics [4]. Their flux linkages and differential inductances vary considerably with the currents throughout the entire operation range. Both changes are caused by magnetic saturation which, additionally, leads to cross-coupling of direct (d)- and quadrature (q)-axis. Due to the complex system description and controller design, the implementation of conventional control approaches may be difficult and sophisticated [5]. In order to achieve good drive performance, the nonlinear saturation effects of RSMs must be properly handled in the control algorithms, e.g., by using nonlinear current control strategies [6], optimal feedforward torque control (OFTC) [7], [8] or model predictive control [9].

Regarding the control of RSMs, two standard approaches are often adopted: direct torque control (DTC) [10], [11] and field oriented control (FOC) [12], [13]. DTC possesses fast torque control dynamics while it results in a variable switching frequency and high torque ripple. On the other hand, FOC (vector control) preserves better steady-state torque response and hence higher system efficiency, but system parameters must be known, e.g., stator resistance, differential inductances, and flux linkages. To ensure good current dynamics, adaptive current controllers [6], [14], [15], [16] are developed where the proportional–integral (PI) controller parameters are updated online with the varying differential inductances. In [14] and [15], stationary and transient inductances are introduced in the system model, which leads to a more complex expression and is physically questionable. The cross-coupling is neglected in [15] to simplify the controller design; consequently, current control performance cannot be ensured in highly saturated conditions. In contrast to that, Hackl et al. [6] propose a nonlinear disturbance compensation method with online tracking of the flux linkages and the differential inductances, so the cross-coupling can be compensated for to achieve good current dynamics for both direct and quadrature components. In [16], the controller structure is achieved via a change of controller state variable, i.e., mapping the current to the flux linkage. Without knowing the differential inductances, the saturation effects are simply taken into account with the nonlinear flux linkages. Hackl [17] introduces a completely parameter-free control method for SMs, which guarantees tracking with prescribed asymptotic and transient control accuracy.

To compensate for the magnetic saturation and cross-coupling effects of RSMs, the nonlinear flux linkages and/or (differential) inductances are usually saved as lookup tables (LUTs). However, all LUTs consume a certain amount of memory and require data interpolation/extrapolation process, which imply burdens on memory and computation in the real-time system. On the contrary, analytical functions are usually parameterized by only a few parameters and are designed to be continuous (or even continuously differentiable) in the whole current range. Hence, they are promising and might be preferable to LUTs in real-time control system with limited storage. Polynomial functions [14], [18] are commonly adopted due to simplicity and wide applicability. In order to improve the fitting performance, higher polynomial orders must be chosen. For example, the seventh-order polynomials are suggested in [18] to approximate the self-axis flux linkage curves of surface mounted PMSMs (SPMSMs), which exhibit almost linear magnetic behavior without saturation. Besides, some prototype functions [19], [20], [21], [22], [23] are specifically designed to naturally incorporate the nonlinear saturation effects. Among all the developed solutions, Su et al. [23] propose analytical flux linkage prototype functions for nonlinear SMs, which, for the whole operation range, 1) achieve good to very good estimation accuracies, 2) preserve continuity and differentiability, and 3) obey the rule of energy conservation (reciprocity rule). Moreover, they easily allow us to derive analytical functions for the self-axis and cross-coupling differential inductances. All these properties are very relevant for current control of RSM, and therefore, these flux linage prototype functions are employed in combination with nonlinear current control system.

In [24] (in German), a nonlinear current control system, based on the concept of input/output (I/O) linearization, has been proposed for RSMs. As it is a model-based approach, the machine's parameters must be known from either finite-element analysis (FEA) or experimental measurements. The I/O linearization technique from the system theory transfers a nonlinear control system to a linear system, i.e., a chain of integrators. Hence, the controller parameters can be designed conveniently with the help of conventional PI controllers and simple pole placement. If the actual current-dependent flux linkages and differential inductances are known and available online, an excellent current control performance over the complete operation range can be achieved.

Main contributions of this article are as follows.

1) A precise definition of the current control objectives and a generic nonlinear machine model and the derivation of the nonlinear current dynamics of RSMs using current-dependent differential inductances and flux linkages.
2) The adaption of the nonlinear I/O-linearization-based current control system from [24] (only available in German) in order to allow for the utilization of flux linkage prototype functions from [23] instead of commonly used LUTs—to do so, the considered RSM must be experimentally identified (as no FEA data are available) and the prototype functions must be designed and fitted properly.
3) The design, fitting, and utilization of generic flux linkage prototype functions for experimentally identified RSMs (instead of RSMs for which FEA data are available as in [23]) to a) compensate for the magnetic saturation and cross-coupling effects and b) obtain analytical functions for the differential inductances for the I/O linearization based current controller (due to continuous differentiability, the differential inductances can be directly derived by analytical differentiation of the flux linkage prototype functions)—by this approach, instead of (at least) five LUTs (with $n \times n$ data points each) solely 6 or 15 parameters must be stored.

4) The effectiveness of the proposed control method is validated by simulation and experimental results.
5) The benefits and potential of utilizing the analytical prototype functions in closed-loop current control are confirmed by a thorough comparison between different updating approaches of the machine nonlinearities (e.g., LUTs, simplified prototype functions, and proposed prototype functions).
6) A detailed evaluation of a) the transient, steady-state, and decoupling control performance of the different approaches by the integral-time-weighted-absolute-error (ITAE) performance measure, b) the required memory, and c) the execution time is presented.

Novel scientific outcomes of this article are as follows.

1) Machine model (over)simplification is still a common practice, although it deteriorates the control performance significantly in particular for nonlinear machines as presented for RSMs in this article.
2) For the very first time, the developed flux linkage prototype functions for RSMs are applied in combination with the nonlinear I/O-linearization-based current control system in order to reduce the required memory to a minimum while control performance and model accuracy are not deteriorated at all. The minimalistic memory requirement and continuous differentiability of the flux linkage prototype functions in combination with the nonlinear control system make the proposed method very attractive for storage-limited (e.g., electromotive or industrial) applications.
3) The prototype functions come with an inherent and excellent extrapolation capability in contrast to the limited range of conventional LUTs, which allows for a safe and reliable over-current operation (as it might occur in real-world applications).

II. MODELING AND PROBLEM STATEMENT

First, the adopted machine model is briefly introduced. Some assumptions are made in the following derivation: 1) mechanical losses (due to friction) and iron losses (due to eddy current and hysteresis effects) are neglected and 2) flux linkages are independent of temperature, speed, and position. Then, the current dynamics of the machine are formulated. Afterward, the resulting control problem is stated and a proper design of the nonlinear current control system is presented.

A. NONLINEAR RSM MODEL

The nonlinear machine model in the rotating (d,q)-reference frame is given by [24]

$$\left.\begin{aligned} \boldsymbol{u}_\mathrm{s}^{dq} &= R_\mathrm{s}\boldsymbol{i}_\mathrm{s}^{dq} + \omega_\mathrm{p}\boldsymbol{J}\boldsymbol{\psi}_\mathrm{s}^{dq}(\boldsymbol{i}_\mathrm{s}^{dq}) + \tfrac{\mathrm{d}}{\mathrm{d}t}\boldsymbol{\psi}_\mathrm{s}^{dq}(\boldsymbol{i}_\mathrm{s}^{dq}) \\ \tfrac{\mathrm{d}}{\mathrm{d}t}\omega_\mathrm{p} &= \tfrac{n_\mathrm{p}}{\Theta_\mathrm{m}}\left(m_\mathrm{m}(\boldsymbol{i}_\mathrm{s}^{dq}) - m_\mathrm{l}\right) \\ \tfrac{\mathrm{d}}{\mathrm{d}t}\phi_\mathrm{p} &= \omega_\mathrm{p} \end{aligned}\right\} \quad (1)$$

where $\boldsymbol{u}_\mathrm{s}^{dq} := (u_\mathrm{s}^d, u_\mathrm{s}^q)^\top$ are the stator voltages, $\boldsymbol{i}_\mathrm{s}^{dq} := (i_\mathrm{s}^d, i_\mathrm{s}^q)^\top$ are the stator currents, $\boldsymbol{\psi}_\mathrm{s}^{dq} := (\psi_\mathrm{s}^d, \psi_\mathrm{s}^q)^\top$ are the flux linkages (which are functions of $\boldsymbol{i}_\mathrm{s}^{dq}$ and stator and rotor temperature, angular velocity, and rotor angle [neglected in this article]) and R_s is the stator resistance. The electrical angular frequency $\omega_\mathrm{p} = n_\mathrm{p}\omega_\mathrm{m}$ rotates the (d,q)-reference frame synchronously, where n_p and ω_m denote the number of pole pairs and the mechanical angular frequency, respectively. ϕ_p is the electrical angle (of the Park transformation). Furthermore, Θ_m is the moment of inertia, while, for $\kappa \in \{2/3, \sqrt{2/3}\}$,[1]

$$m_\mathrm{m}(\boldsymbol{i}_\mathrm{s}^{dq}) = \tfrac{2}{3\kappa^2} n_\mathrm{p}(\boldsymbol{i}_\mathrm{s}^{dq})^\top \boldsymbol{J}\boldsymbol{\psi}_\mathrm{s}^{dq}(\boldsymbol{i}_\mathrm{s}^{dq}) \quad (2)$$

represents the (averaged) electromagnetic torque and m_l is an external load torque.

B. CURRENT DYNAMICS

To further derive the nonlinear current dynamics of RSMs, the last term of the voltage equation in (1) is rewritten as

$$\tfrac{\mathrm{d}}{\mathrm{d}t}\boldsymbol{\psi}_\mathrm{s}^{dq}(\boldsymbol{i}_\mathrm{s}^{dq}) = \tfrac{\partial \boldsymbol{\psi}_\mathrm{s}^{dq}(\boldsymbol{i}_\mathrm{s}^{dq})}{\partial \boldsymbol{i}_\mathrm{s}^{dq}} \tfrac{\mathrm{d}}{\mathrm{d}t}\boldsymbol{i}_\mathrm{s}^{dq} = \boldsymbol{L}_\mathrm{s}^{dq}(\boldsymbol{i}_\mathrm{s}^{dq}) \tfrac{\mathrm{d}}{\mathrm{d}t}\boldsymbol{i}_\mathrm{s}^{dq} \quad (3)$$

where the differential inductance matrix $\boldsymbol{L}_\mathrm{s}^{dq}$ is defined as the (partial) derivative of the flux linkages with respect to the stator currents, i.e.,

$$\boldsymbol{L}_\mathrm{s}^{dq}(\boldsymbol{i}_\mathrm{s}^{dq}) := \begin{bmatrix} \frac{\partial \psi_\mathrm{s}^d(\boldsymbol{i}_\mathrm{s}^{dq})}{\partial i_\mathrm{s}^d} & \frac{\partial \psi_\mathrm{s}^d(\boldsymbol{i}_\mathrm{s}^{dq})}{\partial i_\mathrm{s}^q} \\ \frac{\partial \psi_\mathrm{s}^q(\boldsymbol{i}_\mathrm{s}^{dq})}{\partial i_\mathrm{s}^d} & \frac{\partial \psi_\mathrm{s}^q(\boldsymbol{i}_\mathrm{s}^{dq})}{\partial i_\mathrm{s}^q} \end{bmatrix} := \begin{bmatrix} L_\mathrm{s}^d(\boldsymbol{i}_\mathrm{s}^{dq}) & L_\mathrm{s}^{dq}(\boldsymbol{i}_\mathrm{s}^{dq}) \\ L_\mathrm{s}^{qd}(\boldsymbol{i}_\mathrm{s}^{dq}) & L_\mathrm{s}^q(\boldsymbol{i}_\mathrm{s}^{dq}) \end{bmatrix} \quad (4)$$

where L_s^d & L_s^q and L_s^{dq} & L_s^{qd} are the self-axis and cross-coupling differential inductances, respectively. By obeying the energy conservation rule, the reciprocity relation holds true: The (differential) cross-coupling inductances must equal for all $\boldsymbol{i}_\mathrm{s}^{dq}$, i.e., $L_\mathrm{s}^{dq}(\boldsymbol{i}_\mathrm{s}^{dq}) = L_\mathrm{s}^{qd}(\boldsymbol{i}_\mathrm{s}^{dq})$. Finally, substituting (3) into (1) and solving for the current derivative yields the current dynamics as follows:

$$\tfrac{\mathrm{d}}{\mathrm{d}t}\boldsymbol{i}_\mathrm{s}^{dq} = \boldsymbol{L}_\mathrm{s}^{dq}(\boldsymbol{i}_\mathrm{s}^{dq})^{-1} \cdot \left[\boldsymbol{u}_\mathrm{s}^{dq} - R_\mathrm{s}\boldsymbol{i}_\mathrm{s}^{dq} - \omega_\mathrm{p}\boldsymbol{J}\boldsymbol{\psi}_\mathrm{s}^{dq}(\boldsymbol{i}_\mathrm{s}^{dq})\right] \quad (5)$$

where the inverse of the differential inductance matrix is given by

$$\boldsymbol{L}_\mathrm{s}^{dq}(\boldsymbol{i}_\mathrm{s}^{dq})^{-1} = \frac{1}{\det(\boldsymbol{L}_\mathrm{s}^{dq}(\boldsymbol{i}_\mathrm{s}^{dq}))} \begin{bmatrix} L_\mathrm{s}^q(\boldsymbol{i}_\mathrm{s}^{dq}) & -L_\mathrm{s}^{dq}(\boldsymbol{i}_\mathrm{s}^{dq}) \\ -L_\mathrm{s}^{qd}(\boldsymbol{i}_\mathrm{s}^{dq}) & L_\mathrm{s}^d(\boldsymbol{i}_\mathrm{s}^{dq}) \end{bmatrix}. \quad (6)$$

The (exact) knowledge of the differential inductances and the flux linkages is crucial for the following and all other model-based controller designs; usually, for those, LUTs are used, whereas here, for the very first time, analytical and differentiable flux linkage prototype functions are used.

C. CURRENT CONTROL OBJECTIVE

Control objective of the nonlinear current controllers is stable, fast, and accurate tracking of a given current reference (e.g., obtained by OFTC [7]). Moreover, in order to allow for a simple design of the outer (speed and/or position) control

[1] κ allows for an amplitude or power invariant Clarke transformation.

loops, the closed-loop current dynamics must be identical throughout the whole operation range. The nonlinear current dynamics, as shown in (5), are coupled due to the inverse inductance $\boldsymbol{L}_\mathrm{s}^{dq}(\boldsymbol{i}_\mathrm{s}^{dq})^{-1}$ but also due to the back electromotive force (EMF) term $\omega_\mathrm{p}\boldsymbol{J}\boldsymbol{\psi}_\mathrm{s}^{dq}(\boldsymbol{i}_\mathrm{s}^{dq})$. To alleviate the highly nonlinear characteristics of RSMs, a current control method based on the input–output linearization is proposed as will be explained in detail in the next section. In order to achieve the control objective, few considerations must be taken into account while developing the nonlinear current control system as follows.

1) The modeling correctness must be ensured in accordance with the revisited machine model and current dynamics. Inappropriate model simplification, e.g., assuming constant machine parameters and/or neglecting the saturation and cross-coupling effects, may lead to unsatisfactory control performance.
2) Resistance R_s and flux linkages $\boldsymbol{\psi}_\mathrm{s}^{dq}(\boldsymbol{i}_\mathrm{s}^{dq})$ (which can be obtained by FEA or measurements) must be known, as a model-based control method will be developed. In addition, stator currents $\boldsymbol{i}_\mathrm{s}^{dq}$, mechanical angle ϕ_m, and mechanical angular velocity ω_m are available for feedback.
3) Nonlinear machine characteristics can be stored either in LUTs or represented by analytical prototype functions (which is the proposed method in this article).

III. CURRENT CONTROLLER DESIGN

In this section, the nonlinear controller design based on exact input/output (I/O) linearization and the tuning of the PI controller with anti-windup are discussed. After I/O linearization, the PI controller design is independent of the nonlinear machine parameters.

A. PI CONTROLLER WITH ANTI-WINDUP

It is well known that PI(D) controllers may encounter integral windup due to actuator saturation of the plant. This causes large overshoots and/or oscillations in the closed-loop system response. To prevent the windup problem, a simple and effective anti-windup method utilizing conditional integration [25] is applied. A compact state-space description of the PI controller with anti-windup is given by [24]

$$\left.\begin{aligned}\tfrac{\mathrm{d}}{\mathrm{d}t}\boldsymbol{\xi}_i^{dq} &= f_\mathrm{aw}(\widehat{u},\boldsymbol{u}_\mathrm{s,pi}^{dq})\boldsymbol{e}_\mathrm{s}^{dq}\\ \boldsymbol{u}_\mathrm{s,pi}^{dq}(\boldsymbol{e}_\mathrm{s}^{dq}) &= \boldsymbol{K}_\mathrm{p}^{dq}\boldsymbol{e}_\mathrm{s}^{dq}+\boldsymbol{K}_\mathrm{i}^{dq}\boldsymbol{\xi}_i^{dq}\end{aligned}\right\} \tag{7}$$

with PI controller outputs $\boldsymbol{u}_\mathrm{s,pi}^{dq} := (u_\mathrm{s,pi}^d, u_\mathrm{s,pi}^q)^\top$ (functions of the tracking errors $\boldsymbol{e}_\mathrm{s}^{dq} := (e_\mathrm{s}^d, e_\mathrm{s}^q)^\top$), integral actions $\boldsymbol{\xi}_i^{dq} := (\xi_i^d, \xi_i^q)^\top$ of the PI controllers and the proportional $\boldsymbol{K}_\mathrm{p}^{dq} \in \mathbb{R}^{2\times2}$ and integral $\boldsymbol{K}_\mathrm{i}^{dq} \in \mathbb{R}^{2\times2}$ gain matrices. In the case of current control, the tracking errors

$$\boldsymbol{e}_\mathrm{s}^{dq} := \boldsymbol{i}_\mathrm{s,ref}^{dq} - \boldsymbol{i}_\mathrm{s}^{dq}$$

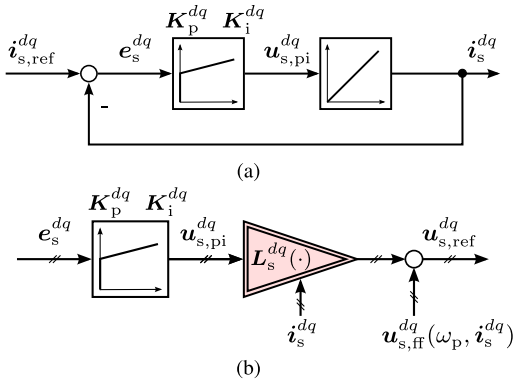

FIGURE 1. Nonlinear current controllers with I/O linearization. (a) Block diagram of the closed-loop current control system. (b) Controller structure.

are defined by the difference between the current references $\boldsymbol{i}_\mathrm{s,ref}^{dq} := (i_\mathrm{s,ref}^d, i_\mathrm{s,ref}^q)^\top$ and the real currents $\boldsymbol{i}_\mathrm{s}^{dq}$. Moreover, the anti-windup decision function

$$f_\mathrm{aw}\left(\widehat{u},\boldsymbol{u}_\mathrm{s,pi}^{dq}\right) = \begin{cases}1, & \|\boldsymbol{u}_\mathrm{s,pi}^{dq}\| < \widehat{u}\\ 0, & \|\boldsymbol{u}_\mathrm{s,pi}^{dq}\| \geq \widehat{u}\end{cases} \tag{8}$$

stops the integration in (7) if the controller output $\boldsymbol{u}_\mathrm{s,pi}^{dq} := (u_\mathrm{s,pi}^d, u_\mathrm{s,pi}^q)^\top$ exceeds the admissible voltage magnitude $\widehat{u}$. According to the applied modulation scheme, for pulsewidth modulation (PWM), the voltage threshold of the inverter is half of the dc-link voltage u_dc, i.e., $\widehat{u} = \frac{u_\mathrm{dc}}{2}$; whereas, for space vector modulation (SVM), it is $\widehat{u} = \frac{u_\mathrm{dc}}{\sqrt{3}}$.

B. BASIC CONCEPT

The basic idea of the I/O linearization is to transform the nonlinear current dynamics of RSMs in (5) into a simple integrator, i.e.,

$$\tfrac{\mathrm{d}}{\mathrm{d}t}\boldsymbol{i}_\mathrm{s}^{dq} = \boldsymbol{u}_\mathrm{s,pi}^{dq}(\boldsymbol{e}_\mathrm{s}^{dq}) \quad \circ\!\!-\!\!\bullet \quad i_\mathrm{s}^{d/q}(s) = \tfrac{1}{s}u_\mathrm{s,pi}^{d/q}(s) \tag{9}$$

whose virtual inputs correspond to the outputs of the current PI controllers $\boldsymbol{u}_\mathrm{s,pi}^{dq}$. To realize (9), a nonlinear feedforward and decoupling of the current dynamics are necessary (see Section III-C).

Neglecting the inverter dynamics and the PI controller nonlinearity [due to the anti-windup decision function in (8)], the closed-loop current control systems [as shown in Fig. 1(a)] consisting of the integrator as in (9) and the PI controller in (7) become, for both d- and q-axis current components, second-order systems of the following form:

$$F_\mathrm{CL}^{d/q}(s) := \frac{i_\mathrm{s}^{d/q}(s)}{i_\mathrm{s,ref}^{d/q}(s)} = \frac{k_\mathrm{p}^{d/q}s + k_\mathrm{i}^{d/q}}{s^2 + k_\mathrm{p}^{d/q}s + k_\mathrm{i}^{d/q}}. \tag{10}$$

Proportional gains $k_\mathrm{p}^{d/q}$ and integral gains $k_\mathrm{i}^{d/q}$ can be tuned by pole placement according to the given desired closed-loop polynomial

$$\chi_\mathrm{ref}^{d/q}(s) = s^2 + 2D^{d/q}\omega_0^{d/q}s + \left(\omega_0^{d/q}\right)^2 \tag{11}$$

where damping $D^{d/q} > 0$ and eigenfrequency $\omega_0^{d/q}$ for d and q components are free design parameters.

A comparison of the coefficients of the desired polynomial in (11) and in the denominator of the closed-loop transfer function (10), i.e.,

$$\chi_{\mathrm{CL}}^{d/q}(s) = s^2 + k_{\mathrm{p}}^{d/q} s + k_{\mathrm{i}}^{d/q} \tag{12}$$

eventually leads to the following tuning rules.

1) For given eigenfrequencies $\omega_0^{d/q}$ (in terms of the d and q-axis bandwidths) and dampings $D^{d/q}$, the controller parameters are obtained as follows:

$$k_{\mathrm{p}}^{d/q} = 2D^{d/q}\omega_0^{d/q} \ \wedge \ k_{\mathrm{i}}^{d/q} = \left(\omega_0^{d/q}\right)^2. \tag{13}$$

2) For given proportional gains $k_{\mathrm{p}}^{d/q} > 0$ (as large as possible) *and* dampings $D^{d/q}$, the integral gains become

$$k_{\mathrm{i}}^{d/q} = (\omega_0^{d/q})^2 \overset{(13)}{=} \left(\frac{k_{\mathrm{p}}^{d/q}}{2D^{d/q}}\right)^2. \tag{14}$$

Normally, an identical choice for d and q components is sufficient, i.e., $k_{\mathrm{p}} = k_{\mathrm{p}}^d = k_{\mathrm{p}}^q$ and $k_{\mathrm{i}} = k_{\mathrm{i}}^d = k_{\mathrm{i}}^q$. Therefore, the controller parameters in (7) can be derived with the form of diagonal matrix

$$\boldsymbol{K}_{\mathrm{p}}^{dq} := \begin{bmatrix} k_{\mathrm{p}} & 0 \\ 0 & k_{\mathrm{p}} \end{bmatrix} \ \wedge \ \boldsymbol{K}_{\mathrm{i}}^{dq} := \begin{bmatrix} k_{\mathrm{i}} & 0 \\ 0 & k_{\mathrm{i}} \end{bmatrix} \tag{15}$$

i.e., $\boldsymbol{K}_{\mathrm{p}}^{dq} = k_{\mathrm{p}}\boldsymbol{I}_2$ and $\boldsymbol{K}_{\mathrm{i}}^{dq} = k_{\mathrm{i}}\boldsymbol{I}_2$.

C. CONTROLLER STRUCTURE

The overall controller structure of the nonlinear current control with I/O linearization is given by

$$\boldsymbol{u}_{\mathrm{s,ref}}^{dq} = \underbrace{\boldsymbol{L}_{\mathrm{s}}^{dq}(\boldsymbol{i}_{\mathrm{s}}^{dq}) \cdot \boldsymbol{u}_{\mathrm{s,pi}}^{dq}(\boldsymbol{e}_{\mathrm{s}}^{dq})}_{\text{nonlinear decoupling and PI controller}} + \underbrace{\boldsymbol{u}_{\mathrm{s,ff}}^{dq}(\omega_{\mathrm{p}}, \boldsymbol{i}_{\mathrm{s}}^{dq})}_{\text{nonlinear feedforward}} \tag{16}$$

and is illustrated in Fig. 1(b) with the stator voltage references $\boldsymbol{u}_{\mathrm{s,ref}}^{dq} := (u_{\mathrm{s,ref}}^d, u_{\mathrm{s,ref}}^q)^\top$ and the feedforward terms $\boldsymbol{u}_{\mathrm{s,ff}}^{dq} := (u_{\mathrm{s,ff}}^d, u_{\mathrm{s,ff}}^q)^\top$. It consists of two parts: 1) the product of the differential inductance matrix $\boldsymbol{L}_{\mathrm{s}}^{dq}(\boldsymbol{i}_{\mathrm{s}}^{dq})$ in (4) and the PI controller output $\boldsymbol{u}_{\mathrm{s,pi}}^{dq}(\boldsymbol{e}_{\mathrm{s}}^{dq})$ in (7) and 2) the additive but nonlinear feedforward term

$$\boldsymbol{u}_{\mathrm{s,ff}}^{dq}(\omega_{\mathrm{p}}, \boldsymbol{i}_{\mathrm{s}}^{dq}) = R_{\mathrm{s}}\boldsymbol{i}_{\mathrm{s}}^{dq} + \omega_{\mathrm{p}}\boldsymbol{J}\boldsymbol{\psi}_{\mathrm{s}}^{dq}(\boldsymbol{i}_{\mathrm{s}}^{dq}). \tag{17}$$

Both parts require an online adaption of the nonlinear flux linkages $\psi_{\mathrm{s}}^d(\boldsymbol{i}_{\mathrm{s}}^{dq})$ and $\psi_{\mathrm{s}}^q(\boldsymbol{i}_{\mathrm{s}}^{dq})$ and the differential inductances $L_{\mathrm{s}}^d(\boldsymbol{i}_{\mathrm{s}}^{dq})$, $L_{\mathrm{s}}^q(\boldsymbol{i}_{\mathrm{s}}^{dq})$ and $L_{\mathrm{s}}^{dq}(\boldsymbol{i}_{\mathrm{s}}^{dq})$ $(= L_{\mathrm{s}}^{qd}(\boldsymbol{i}_{\mathrm{s}}^{dq}))$, which can be stored in LUTs or represented by prototype functions (see Section IV).

With sufficiently high switching frequencies and if inverter nonlinearities and voltage drop on the cables are negligible, the inverter output can be seen as (approximately) equivalent to the stator voltage vector $\boldsymbol{u}_{\mathrm{s}}^{dq}$ at the machine's terminals, i.e., $\boldsymbol{u}_{\mathrm{s}}^{dq} \approx \boldsymbol{u}_{\mathrm{s,ref}}^{dq}$. Under this assumption, the exact I/O linearization of the current dynamics in (5) can be achieved by means of the controller structure in (16) as it compensates the additive disturbance terms in the current dynamics (5) with the help of the feedforward term in (17) and achieves a decoupling of the d and q current components by means of the multiplication $\boldsymbol{L}_{\mathrm{s}}^{dq}(\boldsymbol{i}_{\mathrm{s}}^{dq}) \cdot \boldsymbol{u}_{\mathrm{s,pi}}^{dq}(\boldsymbol{e}_{\mathrm{s}}^{dq})$. As a result, inserting (16) with (17) into (5) finally yields (9) as

$$\begin{aligned}\frac{\mathrm{d}}{\mathrm{d}t}\boldsymbol{i}_{\mathrm{s}}^{dq} &\overset{(5),(16)}{=} \boldsymbol{L}_{\mathrm{s}}^{dq}(\boldsymbol{i}_{\mathrm{s}}^{dq})^{-1} \\ &\quad \cdot \left[\boldsymbol{L}_{\mathrm{s}}^{dq}\boldsymbol{u}_{\mathrm{s,pi}}^{dq} + \boldsymbol{u}_{\mathrm{s,ff}}^{dq} - R_{\mathrm{s}}\boldsymbol{i}_{\mathrm{s}}^{dq} - \omega_{\mathrm{p}}\boldsymbol{J}\boldsymbol{\psi}_{\mathrm{s}}^{dq}(\boldsymbol{i}_{\mathrm{s}}^{dq})\right] \\ &\overset{(17)}{=} \boldsymbol{u}_{\mathrm{s,pi}}^{dq}.\end{aligned}$$

IV. FLUX LINKAGE PROTOTYPE FUNCTION

In this section, the analytical flux linkage prototype functions of RSMs are introduced. The prototype functions are physically motivated and designed to describe the self-axis and cross-coupling saturation effects. Furthermore, the fitting procedure of the prototype function to approximate the nonlinear flux linkages of the considered RSM is discussed.

A. ANALYTICAL PROTOTYPE FUNCTIONS

The RSM flux linkages can be approximated by the following form of analytical prototype functions [23]:

$$\left.\begin{aligned}\widehat{\psi}_{\mathrm{s}}^d(i_{\mathrm{s}}^d, i_{\mathrm{s}}^q) &= \widehat{\psi}_{\mathrm{s,self}}^d(i_{\mathrm{s}}^d) - \widehat{\psi}_{\mathrm{s,cross}}^d(i_{\mathrm{s}}^d, i_{\mathrm{s}}^q) \\ \widehat{\psi}_{\mathrm{s}}^q(i_{\mathrm{s}}^d, i_{\mathrm{s}}^q) &= \widehat{\psi}_{\mathrm{s,self}}^q(i_{\mathrm{s}}^q) - \widehat{\psi}_{\mathrm{s,cross}}^q(i_{\mathrm{s}}^d, i_{\mathrm{s}}^q)\end{aligned}\right\} \tag{18}$$

where $\widehat{\psi}_{\mathrm{s,self}}^d(i_{\mathrm{s}}^d)$ & $\widehat{\psi}_{\mathrm{s,self}}^q(i_{\mathrm{s}}^q)$ and $\widehat{\psi}_{\mathrm{s,cross}}^d(i_{\mathrm{s}}^d, i_{\mathrm{s}}^q)$ & $\widehat{\psi}_{\mathrm{s,cross}}^q(i_{\mathrm{s}}^d, i_{\mathrm{s}}^q)$ represent *self-axis* and *cross-coupling* saturation terms, respectively. The overall flux linkages are obtained by subtracting the cross-coupling saturation terms from the self-axis saturation terms. The cross-coupling saturation terms can be expressed in a general form as

$$\left.\begin{aligned}\widehat{\psi}_{\mathrm{s,cross}}^d(i_{\mathrm{s}}^d, i_{\mathrm{s}}^q) &= \sum_{i=1}^{n} k_i F_i'(i_{\mathrm{s}}^d) G_i(i_{\mathrm{s}}^q) \\ \widehat{\psi}_{\mathrm{s,cross}}^q(i_{\mathrm{s}}^d, i_{\mathrm{s}}^q) &= \sum_{i=1}^{n} k_i F_i(i_{\mathrm{s}}^d) G_i'(i_{\mathrm{s}}^q)\end{aligned}\right\} \tag{19}$$

where $k_1, \ldots, k_n$ are cross-coupling constants, $F_1(i_{\mathrm{s}}^d), \ldots, F_n(i_{\mathrm{s}}^d)$ & $G_1(i_{\mathrm{s}}^q), \ldots, G_n(i_{\mathrm{s}}^q)$ describe the cross-coupling effects and $F_1'(i_{\mathrm{s}}^d), \ldots, F_n'(i_{\mathrm{s}}^d)$ & $G_1'(i_{\mathrm{s}}^q), \ldots, G_n'(i_{\mathrm{s}}^q)$ control the impact of the cross-coupling effect for different current levels on the prototype function; $F_i'(i_{\mathrm{s}}^d) := \frac{\mathrm{d}}{\mathrm{d}i_{\mathrm{s}}^d}F_i(i_{\mathrm{s}}^d)$ and $G_i'(i_{\mathrm{s}}^q) := \frac{\mathrm{d}}{\mathrm{d}i_{\mathrm{s}}^q}G_i(i_{\mathrm{s}}^q)$ denote the respective derivatives of the functions $F_i(i_{\mathrm{s}}^d)$ and $G_i(i_{\mathrm{s}}^q)$. The number n of cross-coupling terms in (19) can be chosen arbitrarily in accordance with given accuracy requirements. Usually, $n = 2$ or $n = 3$ result in sufficient fitting accuracies.

To describe the self-axis saturation effects of the flux linkages, it is pointed out in [23] that the sum of a hyperbolic function and a straight line would be well suited for RSMs. Therefore, the d- and q-axis self-axis saturation terms in (18)

for zero cross-coupling current are defined as follows:

$$\left.\begin{aligned}\widehat{\psi}^{d}_{\mathrm{s,self}}(i^{d}_{\mathrm{s}}) &= a_{\mathrm{d1}}\tanh\left(a_{\mathrm{d2}}i^{d}_{\mathrm{s}}\right)+a_{\mathrm{d3}}i^{d}_{\mathrm{s}}\\ \widehat{\psi}^{q}_{\mathrm{s,self}}(i^{q}_{\mathrm{s}}) &= a_{\mathrm{q1}}\tanh\left(a_{\mathrm{q2}}i^{q}_{\mathrm{s}}\right)+a_{\mathrm{q3}}i^{q}_{\mathrm{s}}\end{aligned}\right\} \tag{20}$$

which mean $\widehat{\psi}^{d}_{\mathrm{s}}(i^{d}_{\mathrm{s}}, i^{q}_{\mathrm{s}}=0)$ and $\widehat{\psi}^{q}_{\mathrm{s}}(i^{d}_{\mathrm{s}}=0, i^{q}_{\mathrm{s}})$, respectively. Both $\widehat{\psi}^{d}_{\mathrm{s,self}}$ and $\widehat{\psi}^{q}_{\mathrm{s,self}}$ are single variant functions, which are dependent only on self-axis current components, with separate function parameters $a_{\mathrm{d1}}, a_{\mathrm{d2}}, a_{\mathrm{d3}}$ and $a_{\mathrm{q1}}, a_{\mathrm{q2}}, a_{\mathrm{q3}}$.

For the cross-coupling saturation characteristics of RSMs, the flux linkages saturate and reduce gradually due to the increase of the cross-coupling currents. Hence, a bell-shaped Gaussian function is a good candidate. In order to achieve a better fitting performance, $n=3$ is chosen in the following, which results in three (modified) Gaussian functions in the cross-coupling terms (19) as follows:

$$\left.\begin{aligned}F_1(i^{d}_{\mathrm{s}}) &= 1-e^{-\left(a_{\mathrm{d4}}\,i^{d}_{\mathrm{s}}\right)^2},\ \ldots,\ F_3(i^{d}_{\mathrm{s}}) = 1-e^{-\left(a_{\mathrm{d6}}\,i^{d}_{\mathrm{s}}\right)^2}\\ G_1(i^{q}_{\mathrm{s}}) &= 1-e^{-\left(a_{\mathrm{q4}}i^{q}_{\mathrm{s}}\right)^2},\ \ldots,\ G_3(i^{q}_{\mathrm{s}}) = 1-e^{-\left(a_{\mathrm{q6}}i^{q}_{\mathrm{s}}\right)^2}\end{aligned}\right\}. \tag{21}$$

These describe how i^{d}_{s} affects ψ^{q}_{s} and how i^{q}_{s} affects ψ^{d}_{s}, respectively. The shared parameters $a_{\mathrm{d4}}, a_{\mathrm{d5}}, a_{\mathrm{d6}}$ and $a_{\mathrm{q4}}, a_{\mathrm{q5}}, a_{\mathrm{q6}}$ affect the widths of the corresponding Gaussian functions. Afterward, the derivatives of (21) are given by

$$\left.\begin{aligned}F'_1(i^{d}_{\mathrm{s}}) &= 2a^2_{\mathrm{d4}}i^{d}_{\mathrm{s}}e^{-\left(a_{\mathrm{d4}}i^{d}_{\mathrm{s}}\right)^2},\ \ldots,\ F'_3(i^{d}_{\mathrm{s}}) = 2a^2_{\mathrm{d6}}i^{d}_{\mathrm{s}}e^{-\left(a_{\mathrm{d6}}i^{d}_{\mathrm{s}}\right)^2}\\ G'_1(i^{q}_{\mathrm{s}}) &= 2a^2_{\mathrm{q4}}i^{q}_{\mathrm{s}}e^{-\left(a_{\mathrm{q4}}i^{q}_{\mathrm{s}}\right)^2},\ \ldots,\ G'_3(i^{q}_{\mathrm{s}}) = 2a^2_{\mathrm{q6}}i^{q}_{\mathrm{s}}e^{-\left(a_{\mathrm{q6}}i^{q}_{\mathrm{s}}\right)^2}\end{aligned}\right\} \tag{22}$$

which control the extent of the cross-coupling saturation effects for different (self-axis) current levels.

B. FITTING

After introducing the flux linkage prototype functions in (18), an effective fitting must be implemented in order to obtain the optimal set of function parameters.

A fitting procedure is designed in a step-by-step manner by fitting (i) the *separate* parameters $a_{\mathrm{d1}}, a_{\mathrm{d2}}, a_{\mathrm{d3}}$ and $a_{\mathrm{q1}}, a_{\mathrm{q2}}, a_{\mathrm{q3}}$ in the self-axis saturation terms $\widehat{\psi}^{d}_{\mathrm{s,self}}$ and $\widehat{\psi}^{q}_{\mathrm{s,self}}$ (20), respectively; (ii) the *shared* parameters $a_{\mathrm{d4}}, a_{\mathrm{d5}}, a_{\mathrm{d6}}$, $a_{\mathrm{q4}}, a_{\mathrm{q5}}, a_{\mathrm{q6}}$ and k_1, k_2, k_3 in the cross-coupling terms $\widehat{\psi}^{d}_{\mathrm{s,cross}}$ and $\widehat{\psi}^{q}_{\mathrm{s,cross}}$ [recall (19), (21), and (22)]; and (iii) the *overall* fitting of *all* parameters

$$\boldsymbol{a}_{\mathrm{dq}} = (a_{\mathrm{d1}},\ldots,a_{\mathrm{d6}},a_{\mathrm{q1}},\ldots,a_{\mathrm{q6}},k_1,k_2,k_3)^{\top}$$

in the flux linkage prototype functions $\widehat{\psi}^{d}_{\mathrm{s}}$ and $\widehat{\psi}^{q}_{\mathrm{s}}$ as in (18). Using the already fitted parameters from steps (i) and (ii) as an initial guess, the optimal parameter vector $\boldsymbol{a}_{\mathrm{dq}}$ can be derived efficiently in step (iii) (usually) with very few iterations and very high fitting accuracy.

C. APPROXIMATION RESULTS

To prove the effectiveness, the flux linkage prototype functions in (18) are used to approximate the real flux linkages of the considered 1.5 kW RSM. Its flux linkages ψ^{d}_{s} and ψ^{q}_{s} are acquired by the state-of-the-art constant speed measurement method with a prescribed current region, i.e., $\|\boldsymbol{i}^{dq}_{\mathrm{s}}\| \le 9.0\,\mathrm{A}$. In Fig. 2, the approximation results using (18) are presented. Fitted d-axis flux linkage $\widehat{\psi}^{d}_{\mathrm{s}}$ and q-axis flux linkage $\widehat{\psi}^{q}_{\mathrm{s}}$ are shown in Fig. 2(a) and (b), respectively. Both flux linkages are smooth due to their continuous differentiability in (18). Moreover, the normalized approximation error

$$\varepsilon^{d/q}_{\mathrm{s}} := \frac{|\psi^{d/q}_{\mathrm{s}} - \widehat{\psi}^{d/q}_{\mathrm{s}}|}{\psi^{d/q}_{\mathrm{s,max}}}\cdot 100\%$$

is introduced to quantify the fitting accuracy, where $\psi^{d/q}_{\mathrm{s,max}}$ are the maximum real values of the d and q flux linkage components. In Fig. 2(c) and (d), the normalized errors $\varepsilon^{d}_{\mathrm{s}}$ and $\varepsilon^{q}_{\mathrm{s}}$ are shown. Both error plots illustrate a (very) high fitting accuracy with less than 1.4 % approximation errors.

Besides, the approximated differential inductances $\widehat{L}^{d}_{\mathrm{s}} = \frac{\partial\widehat{\psi}^{d}_{\mathrm{s}}(\boldsymbol{i}^{dq}_{\mathrm{s}})}{\partial i^{d}_{\mathrm{s}}}$, $\widehat{L}^{q}_{\mathrm{s}} = \frac{\partial\widehat{\psi}^{q}_{\mathrm{s}}(\boldsymbol{i}^{dq}_{\mathrm{s}})}{\partial i^{q}_{\mathrm{s}}}$ and $\widehat{L}^{dq}_{\mathrm{s}} = \frac{\partial\widehat{\psi}^{d}_{\mathrm{s}}(\boldsymbol{i}^{dq}_{\mathrm{s}})}{\partial i^{q}_{\mathrm{s}}} = \frac{\partial\widehat{\psi}^{q}_{\mathrm{s}}(\boldsymbol{i}^{dq}_{\mathrm{s}})}{\partial i^{d}_{\mathrm{s}}}$, derived by analytical differentiation of the flux linkage prototype functions (18), are shown in Fig. 2(e), (f), and (g), respectively. Without designing additional prototype functions for the differential inductances, $\widehat{L}^{d}_{\mathrm{s}}, \widehat{L}^{q}_{\mathrm{s}}$ and $\widehat{L}^{dq}_{\mathrm{s}}$ utilize directly the already fitted parameters in $\boldsymbol{a}_{\mathrm{dq}}$. Moreover, the flux linkage prototype functions also allow for correct extrapolation for both, approximated flux linkages *and* differential inductances, outside the fitted current range as shown in Fig. 2(a), (b), (e), (f), and (g), which is not (directly) feasible with LUTs. Therefore, the proposed flux linkage prototype functions (18) are very attractive for the proposed and any other current control system (16).

V. SIMULATIVE AND EXPERIMENTAL VALIDATION

In this section, both simulations and experiments are conducted in order to demonstrate the effectiveness of the proposed nonlinear current control system using flux linkage prototype functions for RSMs. The nonlinear current controllers (7) with the concept of the exact I/O linearization (9) and the flux linkage prototype functions (18) are implemented in MATLAB/Simulink and at a laboratory setup. The block diagram of the implemented control system is shown in Fig. 3. Key parameters of laboratory setup, implementation, and controllers for simulations and experiments are collected in Table 1.

For the *identical* current reference trajectories, the control performance is evaluated by the following *two* scenarios throughout the whole operation range, i.e., $\|\boldsymbol{i}^{dq}_{\mathrm{s}}\| \le 5.7\,\mathrm{A}$.

1) Operation at idle speed (see simulation [——] and measurement [——] results in Fig. 5).
2) Comparison of the control performance during operation while flux linkages and differential inductances are updated using LUTs [——], simplified prototype functions [——] and the proposed flux linkage prototype functions in (18) [——] (see respective measurement results in Fig. 6).

In order to ease the legibility of Fig. 5, both simulation and measurement results are merged and depicted, where Fig. 5(a)

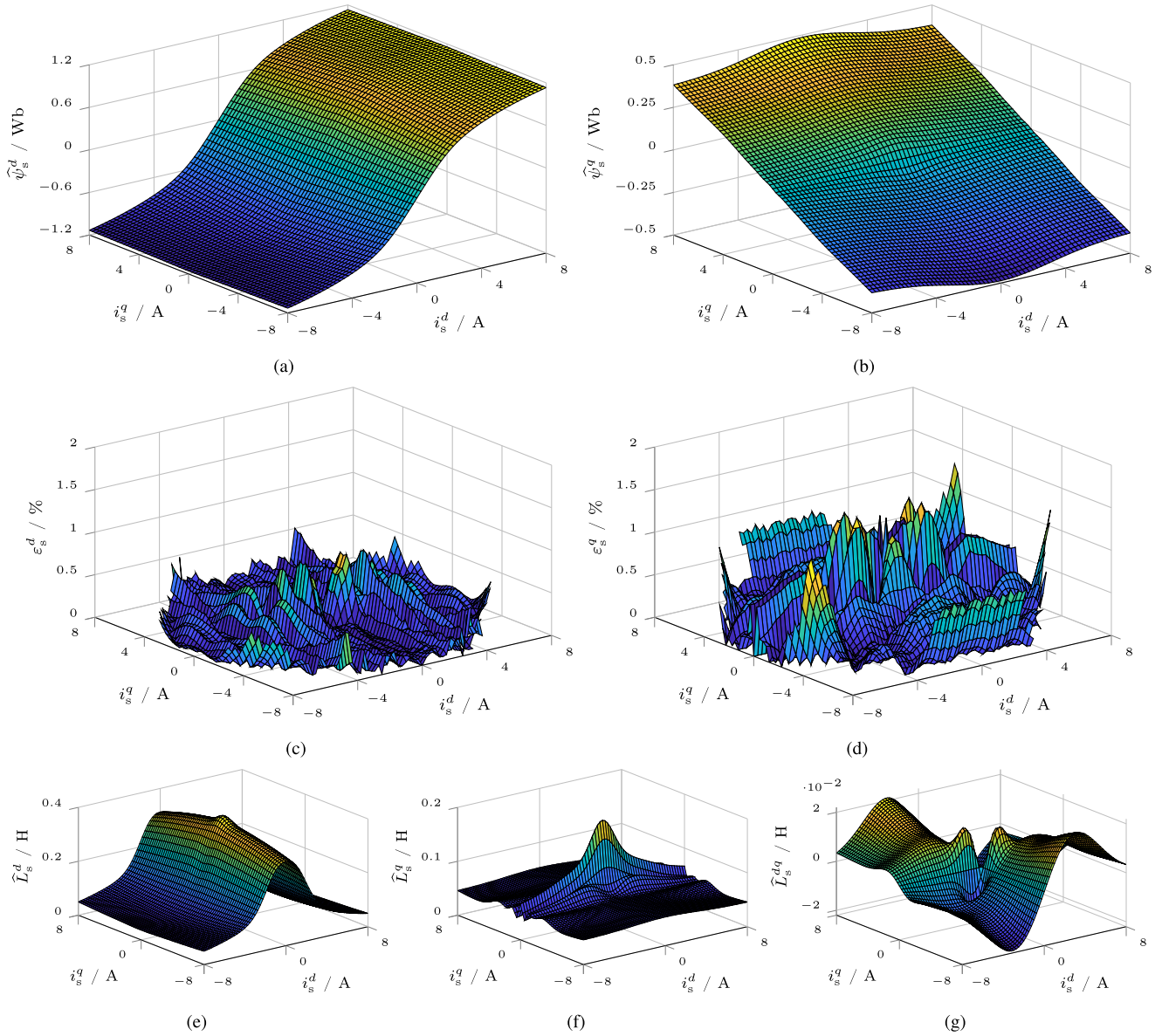

FIGURE 2. Flux linkage approximation results of a 1.5 kW RSM using the flux linkage prototype functions (18). (a) Fitted d-axis flux linkage $\widehat{\psi}_{\mathrm{s}}^{d}$. (b) Fitted q-axis flux linkage $\widehat{\psi}_{\mathrm{s}}^{q}$. (c) Normalized d-axis error $\varepsilon_{\mathrm{s}}^{d}$. (d) Normalized q-axis error $\varepsilon_{\mathrm{s}}^{q}$. (e) Approximated d-axis differential inductance $\widehat{L}_{\mathrm{s}}^{d}$. (f) Approximated q-axis differential inductance $\widehat{L}_{\mathrm{s}}^{q}$. (g) Approximated cross-coupling differential inductance $\widehat{L}_{\mathrm{s}}^{dq}$.

shows the overall duration of the assigned current pattern including direct currents $i_{\mathrm{s,ref}}^{d}$ & i_{s}^{d}, quadrature currents $i_{\mathrm{s,ref}}^{q}$ & i_{s}^{q} and norm of the control input $\|\boldsymbol{u}_{\mathrm{s,ref}}^{dq}\|$ (& inverter voltage limit $\widehat{u}$). Whereas Fig. 5(b), (c), and (d) illustrates the same quantities as Fig. 5(a) but over a smaller time interval (zoomed versions).

A. IMPLEMENTATION

1) SIMULATIONS

Machine model (1) and inverter (for more details see, e.g., [26], Ch. 14]) are built in the stator fixed (α, β)-reference frame. An inverse interpolation method is carried out in simulations to extract the machine stator currents $\boldsymbol{i}_{\mathrm{s}}^{\alpha\beta} := (i_{\mathrm{s}}^{\alpha}, i_{\mathrm{s}}^{\beta})^{\top} = \boldsymbol{T}_{\mathrm{p}}(\phi_{\mathrm{p}})\boldsymbol{i}_{\mathrm{s}}^{dq}$ from the available flux linkage maps, i.e., $\boldsymbol{i}_{\mathrm{s}}^{dq} = f^{-1}(\boldsymbol{\psi}_{\mathrm{s}}^{dq})$. In contrast, the nonlinear PI controllers (7) and also the controller structure (16) with I/O linearization are implemented in the rotating (d,q)-reference frame and output the voltage references $\boldsymbol{u}_{\mathrm{s,ref}}^{dq}$.

As illustrated in Fig. 3, the generated voltage references $\boldsymbol{u}_{\mathrm{s,ref}}^{dq}$ are transformed by the inverse Park and inverse Clarke transformation in order to obtain the voltage references in the (α, β)-reference frame and in the (a, b, c)-reference frame, respectively, i.e., $\boldsymbol{u}_{\mathrm{s,ref}}^{\alpha\beta} := (u_{\mathrm{s,ref}}^{\alpha}, u_{\mathrm{s,ref}}^{\beta})^{\top}$ and $\boldsymbol{u}_{\mathrm{s,ref}}^{abc} := (u_{\mathrm{s,ref}}^{a}, u_{\mathrm{s,ref}}^{b}, u_{\mathrm{s,ref}}^{c})^{\top}$. The implemented regularly sampled

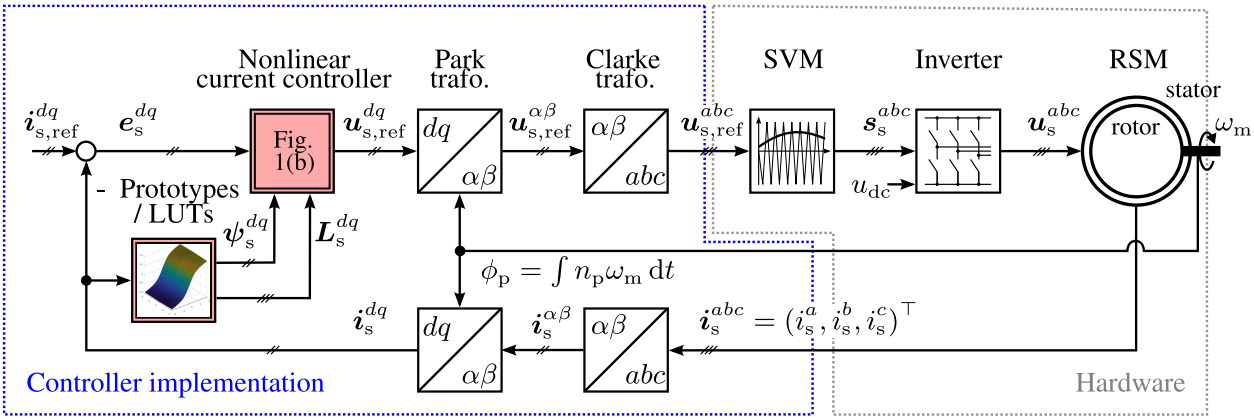

FIGURE 3. Block diagram of the implemented nonlinear current control system with flux linkage prototype functions or LUTs in simulations and experiments.

TABLE 1. Key Parameters of Laboratory Setup, Implementation, and Control System for Simulations and Experiments

RSM	Symbol	Value
Rated power	P_R	1.5 kW
Pole pair	n_p	2
Rated speed	$\omega_{\mathrm{m,R}}$	157.1 rad/s
Rated current	$\widehat{i}_{\mathrm{s,R}}$	5.3 A
Rated voltage	$\widehat{u}_{\mathrm{s,R}}$	326.6 V
Stator resistance	R_s	4.1 Ω
Inertia	Θ_m	8.1×10^{-3} kg m^2
Inverter		
dc link voltage	u_dc	565.0 V
Switching frequency	$f_\mathrm{sw} = 1/T_\mathrm{sw}$	10.0 kHz
Sampling frequency	$f_\mathrm{sam} = 2 \cdot f_\mathrm{sw}$	20.0 kHz
Voltage limit (SVM)	$\widehat{u} = u_\mathrm{dc}/\sqrt{3}$	326.2 V
Nonlinear current control system		
Damping	$D = D^d = D^q$	1.25
Eigenfrequency	$\omega_0 = \omega_0^d = \omega_0^q$	1×10^3 Hz
Proportional gain	$k_\mathrm{p} = k_\mathrm{p}^d = k_\mathrm{p}^q$	2.5×10^3 s^{-1}
Integral gain	$k_\mathrm{i} = k_\mathrm{i}^d = k_\mathrm{i}^q$	1×10^6 s^{-2}

SVM applies the required pulse pattern $\boldsymbol{s}_\mathrm{s}^{abc} := (s_\mathrm{s}^a, s_\mathrm{s}^b, s_\mathrm{s}^c)^\top \in \{0, 1\}^3$ to the voltage source inverter, such that the three-phase stator voltages $\boldsymbol{u}_\mathrm{s}^{abc} := (u_\mathrm{s}^a, u_\mathrm{s}^b, u_\mathrm{s}^c)^\top$ of RSM are produced according to the desired references $\boldsymbol{u}_{\mathrm{s,ref}}^{abc}$. Due to the asymmetrical sampling, the voltage references are updated at both, the positive and negative peak, of the triangular carrier.

2) EXPERIMENTS

At the laboratory setup, as depicted in Fig. 4, the employed RSM under test is not connected to a load machine. Its mechanical angular velocity is thus not kept constant and, on the contrary, will change due to the applied RSM torque. This produces time-varying disturbances, e.g., counter voltages, which must be compensated for dynamically by the proposed current control system. It is implemented in C on the open-source real-time system UltraZohm [27].

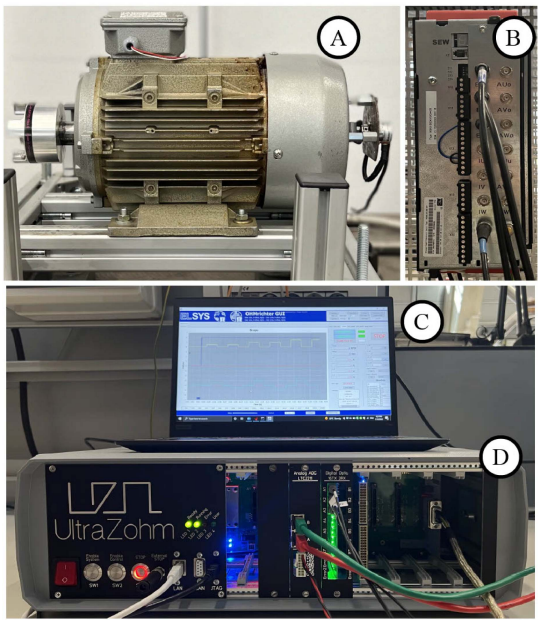

FIGURE 4. Laboratory setup comprising (A) 1.5 kW RSM, (B) SEW inverter, (C) laptop, and (D) UltraZohm real-time system.

For the discrete-time implementation, the nonlinear PI controller (7) with anti-windup (8) is discretized by means of the (simple) explicit Euler method, i.e., $x(t) \approx x[n]$ and $\frac{\mathrm{d}}{\mathrm{d}t}x(t) \approx \frac{x[n]-x[n-1]}{T_\mathrm{sam}}$, where $x[n] := x(nT_\mathrm{sam})$ and the sampling period $T_\mathrm{sam} = \frac{1}{f_\mathrm{sam}} \ll 1$.

B. DISCUSSION OF THE RESULTS

1) SCENARIO (I)—IDLE SPEED OPERATION (SEE FIG. 5)

For a chosen current reference over the whole operation range, the simulation results [——] and the measurement results

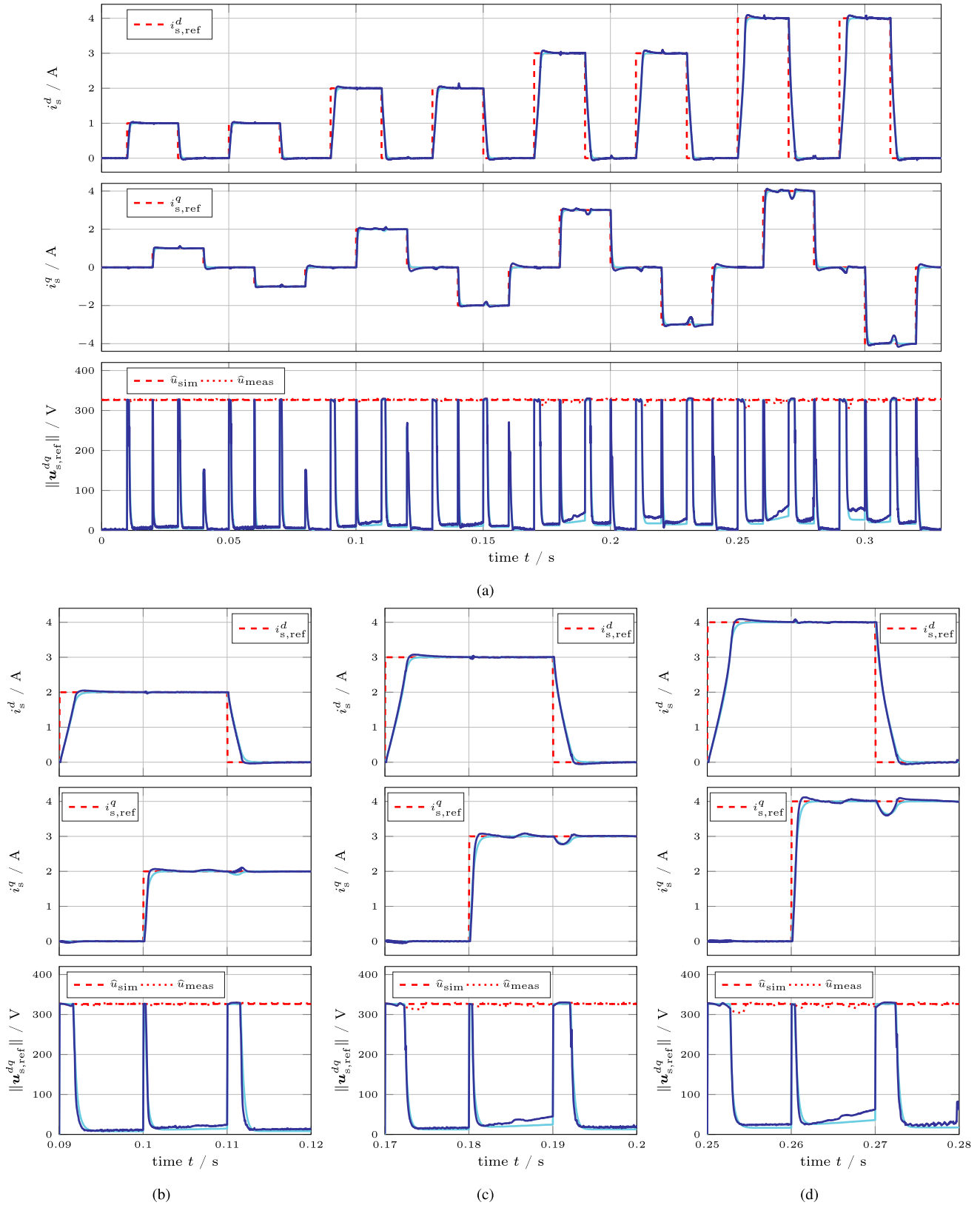

FIGURE 5. Simulation results [——] and measurement results [——] of the nonlinear current control (16) with I/O linearization for the RSM using the flux linkage prototype functions (18) (as depicted in Fig. 2). (a) Entire operation at idle speed. (b) Zoom 1. (c) Zoom 2. (d) Zoom 3.

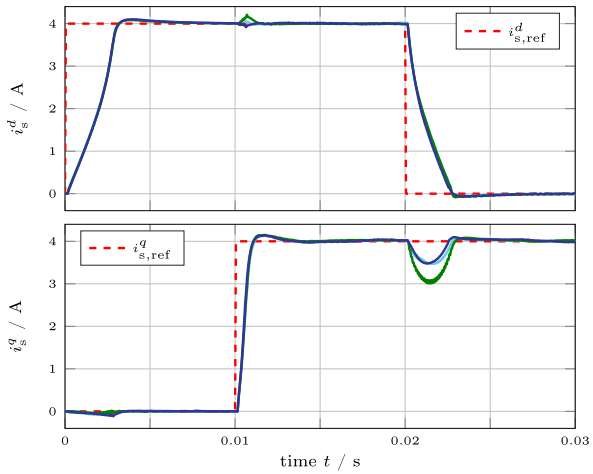

FIGURE 6. Measurement results of the nonlinear current control (16) with I/O linearization for the RSM using 1) five LUTs [——]; 2) simplified prototype functions [——]; and 3) the flux linkage prototype functions (18) [——].

[——] are shown in Fig. 5. It can be seen that simulation and measurement results coincide very well. Thus, the machine's nonlinearities are properly taken into account in the realistic simulation model. The control performance of the proposed current control system is confirmed by its fast and very accurate reference tracking capability. For both d and q components, an (almost) identical transient behavior with similar rise and settling times is ensured. As a consequence, the outer control loops can be easily designed based on simple approximations of the closed-loop current dynamics.

Due to the severe magnetic saturation of RSMs, the flux linkages saturate and thus the differential inductances vary notably with the applied stator currents throughout the entire operation range, as shown in Fig. 2(a) and (b) and Fig. 2(e), (f), and (g), respectively. The developed nonlinear current controllers based on I/O linearization effectively alleviate the effects of the machine's nonlinearities. Especially, the good decoupling behavior in Fig. 5, when d or q currents are at high steady-state values, the other component can rapidly follow a jump of the respective reference value. By means of the introduced controller structure (16), the differential inductance matrix $\boldsymbol{L}_{\mathrm{s}}^{dq}$ allows for 1) direct and quite accurate decoupling and 2) compensation of the magnetic nonlinearities. Moreover, using the flux linkage prototype functions (18) makes memory-expensive LUTs obsolete and allows for a meaning extrapolation.

It can be concluded that the system knowledge is of key importance and can be put to full effect with the proposed control strategy; therefore, the control performance of nonlinear RSMs can be greatly improved.

2) SCENARIO (II)—COMPARISON (SEE FIG. 6)

To show the potential of the utilization of prototype functions in the control system, measurement results are shown in Fig. 6

TABLE 2. Comparison of Integral Time-Weighted Absolute Error (ITAE), Execution Time T_{exe} of an ISR, and Memory (Required Floating-Point Variable Numbers) by Different Compensation Methods (Corresponding to Fig. 6)

Method	ITAE^d (µA s)	ITAE^q (µA s)	T_{exe} (µs)	Memory (variable)
Five LUTs	111.5	52.7	17.9	2000
Simplified prototype functions	112.3	70.7	19.2	6
Flux linkage prototype functions (18)	105.6	50.0	21.3	15

where the flux linkages and the differential inductances of the RSM [in the controller structure (16)] are compensated for and updated in different ways by the following:

1) *five* LUTs with 20 × 20 supporting points and linear interpolation method [——];
2) *simplified* prototype functions without considering the cross-coupling effects [——] (i.e., $\widehat{\psi}_{\mathrm{s}}^{d}(i_{\mathrm{s}}^{d}) = \widehat{\psi}_{\mathrm{s,self}}^{d}(i_{\mathrm{s}}^{d})$ & $\widehat{\psi}_{\mathrm{s}}^{q}(i_{\mathrm{s}}^{q}) = \widehat{\psi}_{\mathrm{s,self}}^{q}(i_{\mathrm{s}}^{q})$ in (20) and $\widehat{L}_{\mathrm{s}}^{dq} = \widehat{L}_{\mathrm{s}}^{qd} = 0$);
3) proposed flux linkage prototype functions (18) [——] (as presented in Fig. 2).

Although different controller tunings might lead to different control performances, the tuning is kept identical for all approaches in order to achieve a fair comparison of the control performances and different compensation methods. Moreover, it is important to note that, due to the exact I/O-linearization approach, a more aggressive tuning will not lead to, e.g., a better decoupling performance. The control performance is mostly affected by precise system knowledge requiring high-resolution LUTs or well-fitted flux linkage prototype functions considering magnetic saturation *and* cross-coupling effects. It can be observed that the results using LUTs or the proposed prototype functions as in (18), both considering cross-coupling effects, are similar and lead to a very good control and decoupling performance. Direct current i_{s}^{d} and quadrature current i_{s}^{q} are decoupled and track the reference steps very quickly and accurately. In contrast to that, when solely the simplified prototype functions *without* consideration of the cross-coupling effects are used, the decoupling performance is significantly deteriorated at $t = 0.01\,\mathrm{s}$ for i_{s}^{d} and $t = 0.02\,\mathrm{s}$ for i_{s}^{q}, whereas rise time and steady-state performance are similar to the other two approaches. Moreover, in particular at $t = 0.02\,\mathrm{s}$ for i_{s}^{q}, undesired current ripples are visible, which are due to the insufficient amount of data points of the used LUTs and the insufficient interpolation accuracy (with 400 data points each). In conclusion, the magnetic saturation and cross-coupling effects must be taken into account in the nonlinear current control system design to achieve an improved and decoupled control performance.

For further comparisons of the measurement results in Fig. 6, Table 2 lists several parameters of the different nonlinear current control algorithms that were evaluated by 1) the integral time-weighted absolute error (ITAE) performance

measure

$$\mathrm{ITAE}^{d/q}\left(e_{\mathrm{s}}^{d/q}, 0, t_{\mathrm{end}}\right) := \int_0^{t_{\mathrm{end}}} \tau \left| e_{\mathrm{s}}^{d/q}(\tau) \right| \mathrm{d}\tau$$

for both d and q components and $t_{\mathrm{end}} = 0.03\,\mathrm{s}$; 2) (average) execution time T_{exe} of an Interrupt Service Routine (ISR); and 3) number of required floating-point variables (parameters) saved in the memory. As already observed in Fig. 6, using the simplified prototype functions results in the worst control performance with the highest values for ITAE^d and ITAE^q. However, the least memory is needed, i.e., six parameters for the self-axis saturation functions (20). When it comes to the comparison between LUTs and flux linkage prototype functions (18), the ITAE values when using (18) are slightly better than those when LUTs are used. This might be a result from insufficient supporting points of the saved LUTs and/or the inaccurate inter/extrapolation of LUTs. Using the prototype functions (18) requires (slightly) longer execution time due to the chosen hyperbolic and (modified) Gaussian functions, whereas—most importantly—the stored amount of data (variables/parameters) can significantly be reduced to only 15 parameters in contrast to 2000 when LUTs are used. The saved storage can, therefore, be utilized to compensate for further nonlinear effects such as inverter nonlinearities or iron losses.

The potential of using flux linkage prototype functions in control is confirmed by simulation and measurement results. With high approximation accuracy and continuous differentiability, the (fitted) flux linkages and (approximated) differential inductances can be utilized directly in the proposed current control scheme and make LUTs obsolete. Apart from that, the prototype functions can also be used to compensate for machine parameters in OFTC [7], which will be presented in a follow-up publication.

VI. CONCLUSION

In this article, a nonlinear current control system for RSMs with I/O linearization and analytical flux linkage prototype functions was proposed. Based on the idea of I/O linearization, the nonlinear control system can be simplified to an integrator for both current components. Hence, the PI controller design is independent of the machine parameters and can be achieved simply by pole placement. For the designed controller structure, the nonlinear flux linkages and differential inductances must be updated online at each sampling instant. To do so, analytical flux linkage prototype functions with few parameters were utilized instead of LUTs. Thanks to their excellent fitting accuracies, the approximated flux linkages and differential inductances can be used directly. Finally, the presented nonlinear current controllers for RSMs were validated by simulations and at a laboratory setup. Simulation and measurement results matched nicely and illustrated the very good control performance: The closed-loop current dynamics were shown to have 1) fast and accurate current reference tracking capabilities and 2) an (almost) identical closed-loop response over the entire operation range. In addition, by comparing different solutions for making the machine parameters available to the control system, the full advantages of the flux linkage prototype functions were confirmed as a (very) good control performance and much lower memory requirements in the real-time system are achieved.

ACKNOWLEDGMENT

The authors are deeply indebted to Prof. Maarten Kamper (Stellenbosch University, South Africa) for designing and manufacturing the prototype RSM.

REFERENCES

[1] S. Staudt, A. Stock, T. Kowalski, J. Teigelkötter, and K. Lang, "Raw data based model and high dynamic control concept for traction drives powered by synchronous reluctance machines," in *Proc. IEEE Workshop Elect. Mach. Des. Control Diagnosis*, 2015, pp. 204–209.

[2] E. Castagnaro and N. Bianchi, "High-speed synchronous reluctance motor for electric-spindle application," in *Proc. IEEE Int. Conf. Elect. Mach.*, 2020, pp. 2419–2425.

[3] G. V. Kumar, C.-H. Chuang, M.-Z. Lu, and C.-M. Liaw, "Development of an electric vehicle synchronous reluctance motor drive," *IEEE Trans. Veh. Technol.*, vol. 69, no. 5, pp. 5012–5024, May 2020.

[4] A. Vagati, M. Pastorelli, F. Scapino, and G. Franceschini, "Impact of cross saturation in synchronous reluctance motors of the transverse-laminated type," *IEEE Trans. Ind. Appl.*, vol. 36, no. 4, pp. 1039–1046, Jul./Aug. 2000.

[5] T. Lubin, H. Razik, and A. Rezzoug, "Magnetic saturation effects on the control of a synchronous reluctance machine," *IEEE Trans. Energy Convers.*, vol. 17, no. 3, pp. 356–362, Sep. 2002.

[6] C. M. Hackl, M. J. Kamper, J. Kullick, and J. Mitchell, "Current control of reluctance synchronous machines with online adjustment of the controller parameters," in *Proc. IEEE 25th Int. Symp. Ind. Electron.*, 2016, pp. 153–160.

[7] H. Eldeeb, C. M. Hackl, L. Horlbeck, and J. Kullick, "A unified theory for optimal feedforward torque control of anisotropic synchronous machines," *Int. J. Control*, vol. 91, no. 10, pp. 2273–2302, 2018.

[8] C. Hackl, J. Kullick, and N. Monzen, "Generic loss minimization for nonlinear synchronous machines by analytical computation of optimal reference currents considering copper and iron losses," in *Proc. 22nd IEEE Int. Conf. Ind. Technol.*, 2021, pp. 1348–1355.

[9] A. Zanelli, J. Kullick, H. M. Eldeeb, G. Frison, C. M. Hackl, and M. Diehl, "Continuous control set nonlinear model predictive control of reluctance synchronous machines," *IEEE Trans. Control Syst. Technol.*, vol. 30, no. 1, pp. 130–141, Jan. 2022.

[10] R. Lagerquist, I. Boldea, and T. J. E. Miller, "Sensorless-control of the synchronous reluctance motor," *IEEE Trans. Ind. Appl.*, vol. 30, no. 3, pp. 673–682, May/Jun. 1994.

[11] S. Wiedemann and A. Dziechciarz, "Comparative evaluation of DTC strategies for the synchronous reluctance machine," in *Proc. IEEE 10th Int. Conf. Ecol. Veh. Renewable Energies*, 2015, pp. 1–5.

[12] T. Matsuo and T. A. Lipo, "Field oriented control of synchronous reluctance machine," in *Proc. IEEE Power Electron. Specialist Conf.*, 1993, pp. 425–431.

[13] J. E. Fletcher, B. W. Williams, and T. C. Green, "Efficiency aspects of vector control applied to synchronous reluctance motors," in *Proc. IEEE Ind. Appl. Conf. 13th IAS Annu. Meeting*, 1995, pp. 294–300.

[14] A. Kilthau and J. M. Pacas, "Appropriate models for the control of the synchronous reluctance machine," in *Proc. IEEE Ind. Appl. Conf. 37th IAS Annu. Meeting*, 2002, pp. 2289–2295.

[15] I. Z. Petrić et al., "A robust current controller design method for highly nonlinear synchronous reluctance motors," in *Proc. 10th Int. Conf. Power Electron. Mach. Drives*, 2020, pp. 104–109.

[16] H. A. A. Awan, S. E. Saarakkala, and M. Hinkkanen, "Flux-linkage-based current control of saturated synchronous motors," *IEEE Trans. Ind. Appl.*, vol. 55, no. 5, pp. 4762–4769, Sep./Oct. 2019.

[17] C. M. Hackl, "Current PI-funnel control with anti-windup for synchronous machines," in *Proc. 54th IEEE Conf. Decis. Control*, 2015, pp. 1997–2004.

[18] M. Seilmeier and B. Piepenbreier, "Identification of steady-state inductances of PMSM using polynomial representations of the flux surfaces," in *Proc. 39th Annu. Conf. IEEE Ind. Electron. Soc.*, 2013, pp. 2899–2904.
[19] Z. Qu, T. Tuovinen, and M. Hinkkanen, "Inclusion of magnetic saturation in dynamic models of synchronous reluctance motors," in *Proc. 20th Int. Conf. Elect. Mach.*, 2012, pp. 994–1000.
[20] N. Bedetti, S. Calligaro, and R. Petrella, "Stand-still self-identification of flux characteristics for synchronous reluctance machines using novel saturation approximating function and multiple linear regression," *IEEE Trans. Ind. Appl.*, vol. 52, no. 4, pp. 3083–3092, Jul./Aug. 2016.
[21] S.-W. Su, R. Kennel, and C. M. Hackl, "Analytical flux linkage approximation prototypes for reluctance synchronous machines," in *Proc. Int. Symp. Power Electron. Elect. Drives Automat. Motion*, 2020, pp. 91–96.
[22] A. Accetta, M. Cirrincione, M. Pucci, and A. Sferlazza, "Space-vector state dynamic model of SynRM considering self- and cross-saturation and related parameter identification," *IET Elect. Power Appl.*, vol. 14, no. 14, pp. 2798–2808, Dec. 2020.
[23] S.-W. Su, C. M. Hackl, and R. Kennel, "Analytical prototype functions for flux linkage approximation in synchronous machines," *IEEE Open J. Ind. Electron. Soc.*, vol. 3, pp. 265–282, Mar. 2022.
[24] C. Hackl, J. Kullick, and P. Landsmann, "Nichtlineare stromregelverfahren für reluktanz-synchronmaschinen," in *Elektrische Antriebe – Regelung von Antriebssystemen*, D. Schröder and J. Böcker, Eds. Berlin, Germany: Springer-Verlag, 2021.
[25] Y. Peng, D. Vrancic, and R. Hanus, "Anti-windup, bumpless, and conditioned transfer techniques for PID controllers," *IEEE Control Syst. Mag.*, vol. 16, no. 4, pp. 48–57, Aug. 1996.
[26] C. Hackl, *Non-Identifier Based Adaptive Control in Mechatronics*. Berlin, Germany: Springer, 2017.
[27] E. Liegmann, T. Schindler, P. Karamanakos, A. Dietz, and R. Kennel, "UltraZohm—An open-source rapid control prototyping platform for power electronic systems," in *Proc. Int. Aegean Conf. Elect. Mach. Power Electron. Int. Conf. Optim. Elect. Electron. Equip.*, 2021, pp. 445–450.

SHIH-WEI SU was born in 1993 in Taichung, Taiwan. He received the B.Sc. degree from the National Taipei University of Technology, Taipei, Taiwan, in 2015, and the M.Sc. degree from National Tsing Hua University, Hsinchu, Taiwan, in 2017, both in electrical engineering. He is currently working toward the Ph.D. degree in electrical engineering with the Chair of High-Power Converter Systems, formerly Chair of Electrical Drive Systems and Power Electronics, Technical University of Munich, Munich, Germany.

His research interests include power electronics, electrical drives, modeling of electrical machines, and encoderless control.

HANNES BÖRNGEN (Student Member, IEEE) received the B.Sc. and M.Sc. degrees in electrical engineering, majoring in power electronics, from Friedrich-Alexander-Universität Erlangen-Nürnberg, Erlangen, Germany, in 2013 and 2015, respectively. He is currently working toward the Ph.D. degree in electrical engineering from the Technical University of Munich, Munich, Germany.

Since 2016, he has been a Research Assistant with the Chair of High-Power Converter Systems, formerly Chair of Electrical Drive Systems and Power Electronics, Technical University of Munich, Munich, Germany. His research focuses on encoderless control of synchronous electrical machines as well as power electronics.

CHRISTOPH M. HACKL (Senior Member, IEEE) was born in 1977, in Mannheim, Germany. He received the the B.Sc. degree in electrical engineering (with focus on mechatronics and systems and control) from the Technical University of Munich (TUM), Munich, Germany, and the University of Wisconsin-Madison, Madison, WI, USA, in 2003, and the Dipl.-Ing. and Dr.-Ing. (Ph.D.) degrees in electrical engineering from TUM in 2004 and 2012, respectively.

Since 2004, he has been teaching electrical drives, power electronics, and mechatronic and renewable energy systems. Since 2014, he has been the Head of the research group "Control of Renewable Energy Systems (CRES)," TUM. In 2018, he became a Professor for Electrical Machines and Drives and the Head of the "Laboratory for Mechatronic and Renewable Energy Systems (LMRES)," Hochschule München (HM) University of Applied Sciences, Germany. In 2019, he completed his habilitation on "Mechatronic and Renewable Energy Systems" and cofounded the research Institute for Sustainable Energy Systems (ISES), HM, which he coheads since then. His research interests include nonlinear, adaptive, and optimal control and design of electrical drives, and mechatronic and renewable energy systems.

RALPH KENNEL (Senior Member, IEEE) was born in Kaiserslautern, Germany, in 1955. He received the Diploma and Dr. Ing. (Ph.D.) degrees in electrical engineering from the University of Kaiserslautern, Kaiserslautern, Germany, in 1979 and 1984, respectively.

From 1983 to 1999, he worked on several positions with Robert BOSCH GmbH (Germany). Until 1997, he was responsible for the development of servo drives. From 1994 to 1999, he was a Visiting Professor with the University of Newcastle-upon-Tyne, Newcastle-upon-Tyne, U.K. From 1999 to 2008, he was a Professor of Electrical Machines and Drives with Wuppertal University, Wuppertal, Germany. Since 2008, he has been a Professor of Electrical Drive Systems and Power Electronics with the Technical University of Munich, Munich, Germany. His current main interests include renewable energy systems, sensorless control of ac drives, predictive control of power electronics, and hardware-in-the-loop systems.

Dr. Kennel is a Fellow of the IEE and a Chartered Engineer in the U.K. within IEEE. He is a Treasurer of the Germany Section as well as the ECCE Global Partnership Chair of the Power Electronics Society. He is an Associate Editor for the IEEE TRANSACTIONS ON POWER ELECTRONICS.